Subduction of a buoyant plateau at the Manila Trench: Tomographic evidence and geodynamic implications

Article *in* Geochemistry Geophysics Geosystems · January 2016

DOI: 10.1002/2015GC006201

CITATIONS
0

READS
268

3 authors:

Jianke Fan
Chinese Academy of Sciences
5 PUBLICATIONS **4** CITATIONS
SEE PROFILE

Dapeng Zhao
Tohoku University
281 PUBLICATIONS **13,243** CITATIONS
SEE PROFILE

Dongdong Dong
Chinese Academy of Sciences
4 PUBLICATIONS **1** CITATION
SEE PROFILE

AGU PUBLICATIONS

Geochemistry, Geophysics, Geosystems

RESEARCH ARTICLE
10.1002/2015GC006201

Subduction of a buoyant plateau at the Manila Trench: Tomographic evidence and geodynamic implications

Jianke Fan[1,2], Dapeng Zhao[3], and Dongdong Dong[1,2]

[1]Key Laboratory of Marine Geology and Environment, Institute of Oceanology, Chinese Academy of Sciences, Qingdao, China, [2]Laboratory for Marine Geology, Qingdao National Laboratory for Marine Science and Technology, Qingdao, China, [3]Department of Geophysics, Tohoku University, Sendai, Japan

Key Points:
- Tomography shows partial subduction of a buoyant plateau at the Manila trench
- Separation and convergence of western and eastern volcanic chains in the Luzon Arc are explained
- The subduction along the Manila Trench stops at ~22°N and collision develops northward

Correspondence to:
J. Fan
fanjianke@qdio.ac.cn

Citation:
Fan, J., D. Zhao, and D. Dong (2016), Subduction of a buoyant plateau at the Manila Trench: Tomographic evidence and geodynamic implications, *Geochem. Geophys. Geosyst.*, *17*, doi:10.1002/2015GC006201.

Received 24 NOV 2015
Accepted 13 JAN 2016
Accepted article online 19 JAN 2016

Abstract We determined P-wave tomographic images by inverting a large number of arrival-time data from 2749 local earthquakes and 1462 teleseismic events, which are used to depict the three-dimensional morphology of the subducted Eurasian Plate along the northern segment of the Manila Trench. Dramatic changes in the dip angle of the subducted Eurasian Plate are revealed from the north to the south, being consistent with the partial subduction of a buoyant plateau beneath the Luzon Arc. Slab tears may exist along the edges of the buoyant plateau within the subducted plate induced by the plateau subduction, and the subducted lithosphere may be absent at depths greater than 250 km at ~19°N and ~21°N. The subducted buoyant plateau is possibly oriented toward NW-SE, and the subducted plate at ~21°N is slightly steeper than that at ~19°N. These results may explain why the western and eastern volcanic chains in the Luzon Arc are separated by ~50 km at ~18°N, whereas they converge into a single volcanic chain northward, which may be related to the oblique subduction along the Manila Trench caused by the northwestern movement of the Philippine Sea Plate. A low-velocity zone is revealed at depths of 20–200 km beneath the Manila Accretionary Prism at ~22°N, suggesting that the subduction along the Manila Trench may stop there and the collision develops northward. The Taiwan Orogeny may originate directly from the subduction of the buoyant plateau, because the initial time of the Taiwan Orogeny is coincident with that of the buoyant plateau subduction.

1. Introduction

The Manila Trench and the Luzon Arc were created by the subduction of the Eurasian Plate beneath the Philippine Sea Plate since the early Miocene [*Taylor and Hayes*, 1983; *Hayes and Lewis*, 1984]. The collision between the Eurasian Plate and the Luzon Arc has resulted in the Taiwan Island (Figure 1) [e.g., *Stephan et al.*, 1986; *Suppe*, 1988; *Teng*, 1990]. So far, many studies relevant to the Taiwan orogeny have been made [e.g., *Suppe*, 1981, 1984; *Wu* et al., 1997; *Liu* et al., 2000; *Willett et al.*, 2003; *Lee et al.*, 2006; *Beyssac et al.*, 2007; *Kaus et al.*, 2008]. It is widely accepted that the collision has propagated southwestward through time [*Suppe*, 1981] due to the northwestern movement of the Philippine Sea Plate, implying that it changes from mature collision in northern Taiwan to an early stage of collision in southern Taiwan, whereas the areas between Taiwan and Luzon represent a subduction zone before collision.

One conspicuous feature in the bathymetric map is the collision between the trench with two bathymetric highs, including a fossil ridge and a buoyant plateau southwest of Taiwan (Figure 1). The subduction of the fossil ridge in the South China Sea has been demonstrated by seismic tomography [*Fan et al.*, 2015], whereas the subduction of the buoyant plateau, comprised of an extended to hyperextended continental crust, was revealed by seismic reflection and wide-angle seismic data obtained by the TAIGER (Taiwan Integrated Geodynamics Research) project [e.g., *Lester et al.*, 2013; *McIntosh et al.*, 2013; *Eakin et al.*, 2014]. The subduction of the buoyant plateau is considered to be the origin of the Central Ranges in Taiwan [*McIntosh et al.*, 2013]. The subduction of the fossil ridge and the buoyant plateau may have caused the subduction of the Eurasian Plate at a shallow angle, the sharp bend in the trench axis, and the complicated deformation pattern on the overriding plate, including significant variations among the volcanoes in the Luzon Arc (Figure 1) [*Bautista et al.*, 2001].

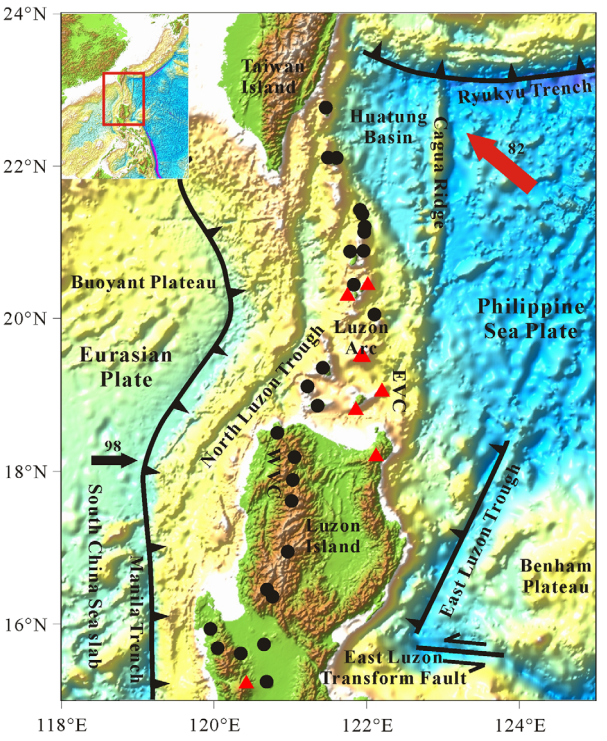

Figure 1. Tectonic background in and around the northern segment of the Manila subduction zone. The bathymetric data are from *Smith and Sandwell* [1997]. The saw-toothed lines denote trench axes of subduction zones, and the solid line denotes a fault. The bold red arrow and the number beside it indicate the moving direction and rate (mm/yr) of the Philippine Sea Plate with respect to the Eurasian Plate [*Yu and Kuo*, 1999]. The bold black arrow and the number beside it denote the subduction direction and rate (mm/yr) of the South China Sea slab [*Rangin et al*., 1999]. The black dots represent inactive volcanoes, whereas the red triangles denote active volcanoes. WVC, the western volcanic chain; EVC, the eastern volcanic chain. The inset map shows the location of the study area (red box).

Although the crustal structure in this area has been well studied, the morphology of the subducted Eurasian Plate beneath the northern segment of the Manila Trench (i.e., south of Taiwan Island) is still controversial. Previous tomographic studies have suggested that the Eurasian lithosphere has subducted down to a depth of ~670 km beneath southern Taiwan [e.g., *Bijwaard et al*., 1998; *Lallemand et al*., 2001; *Koulakov et al*., 2014], but these tomographic models have a lower resolution (~120 km at depths of 0–200 km and ~200 km at depths of 200–710 km). Therefore, it is crucial and necessary to determine a high-resolution tomography of the crust and upper mantle beneath the region for a better understanding of the structural heterogeneities and geodynamics. In this work, we apply seismic tomography to study the deep velocity structure of the region. Our present results provide new constrains on the subduction of the buoyant plateau, the plate interactions and arc magmatism, in particular, the formation of Taiwan Island, the transition from subduction to collision, and the tectonic evolution of the study region.

2. Data and Method

We used P-wave arrival-time data of local earthquakes and teleseismic events selected from the International Seismological Centre (ISC) Bulletin from 1960 to 2011. The earthquakes used in this study are selected on the basis of the following criteria: (1) each earthquake was recorded by more than four seismic stations in the study region (Figure 2a); (2) the absolute value of the travel-time residuals is smaller than 5 s; and (3) teleseismic events are located at an epicentral distance of 30°–100° from the center of the study area, in order to avoid the effects of the complex structures of the core-mantle boundary and the upper mantle outside the study region [*Zhao et al*., 1994, 2013]. As a result, our data set contains 84,941 arrival times from 2749 local earthquakes and 7965 arrival times from 1462 teleseismic events, which are used in the tomographic inversion. Figure 2 shows the distribution of the earthquakes and seismic stations used in this study.

The deep structure of the upper mantle beneath the study region is mainly constrained by the teleseismic data; therefore, the accuracy and distribution of these data are essential. In order to get rid of the effects of hypocentral mislocation and origin times of the teleseismic events, as well as the complex structures outside the study volume, we use relative travel-time residuals of teleseismic events in the tomographic inversion [*Zhao et al*., 1994, 2013]. For each teleseismic event, the relative travel-time residuals are obtained by removing the mean residual over all recording stations from the raw residuals which are computed by subtracting the origin time and the theoretical travel times for the iasp91 Earth Model [*Kennett and Engdahl*, 1991] from the observed arrival times.

The tomographic method of *Zhao et al*. [1994, 2012] for local and teleseismic travel-time joint inversion is used to determine a 3-D P-wave velocity model beneath the study area. For the local events, their hypocenters are relocated using the Adaptive Quantum Genetic Algorithm [*Shi et al*., 2009], and their raw travel-time residuals are used in the tomographic inversion. In contrast, the relative travel-time residuals of the teleseismic

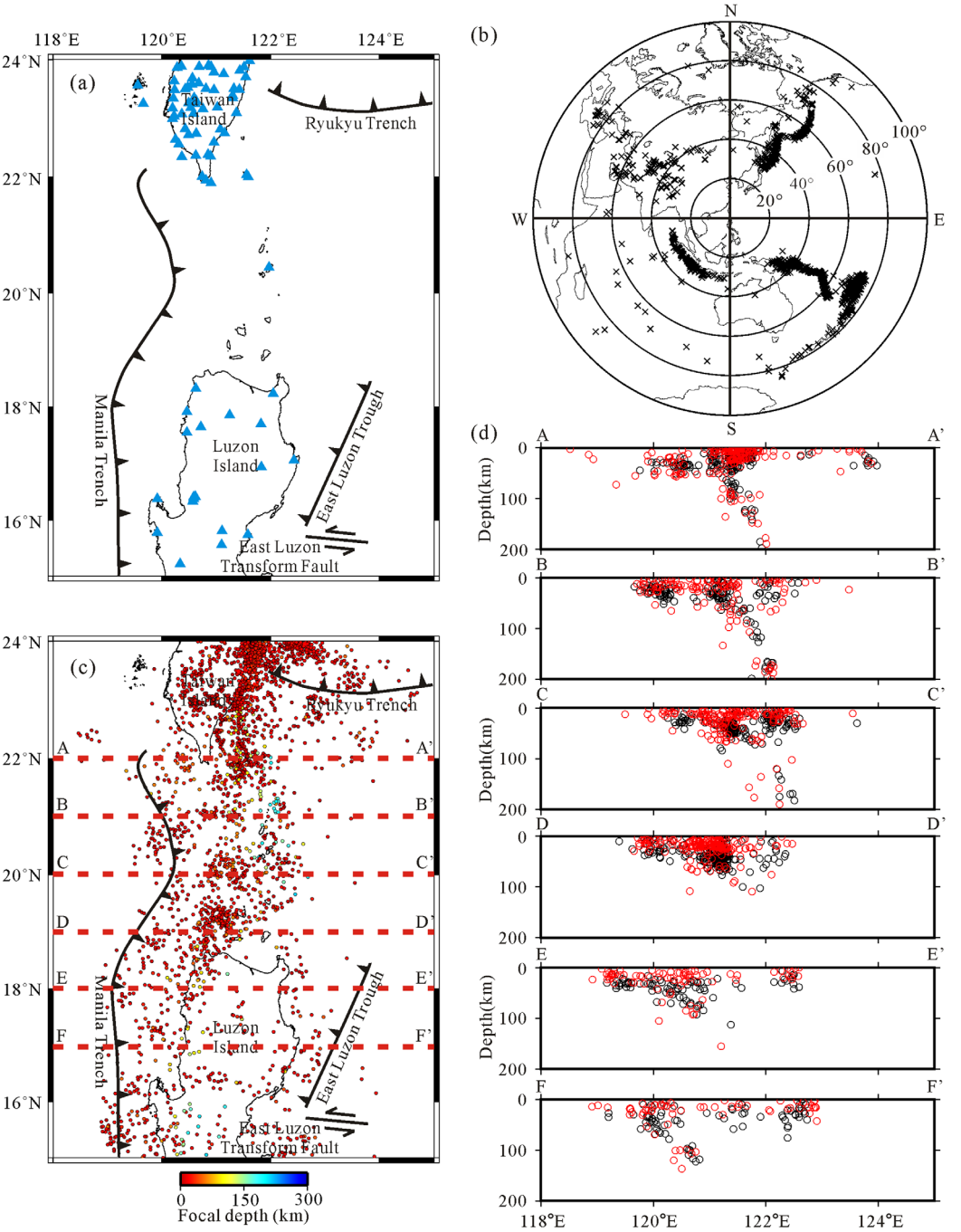

Figure 2. Distribution of (a) seismic stations (blue triangles), (b) teleseismic events (black crosses), and (c) local earthquakes used in this study, (d) East-west vertical cross sections of the local events within a width of 30 km along each of the profiles shown in (c) (red-dashed lines). The colors in Figure 2c denote the focal depths. The black and red circles in Figure 2d denote the local events before and after relocation, respectively. The other symbols are the same as those in Figure 1.

events are used in the tomographic inversion. The LSQR algorithm [*Paige and Saunders*, 1982] with damping and smoothing regularizations [*Zhao et al.*, 1994, 2012] is used to conduct the tomographic inversion.

3. Model Parameterization and Inversion

A one-dimensional (1-D) starting model is derived from the models CRUST1.0 [*Laske et al.*, 2013] and iasp91 [*Kennett and Engdahl*, 1991]. Because of the significant lateral variations in the Conrad (4–18.5 km) and the

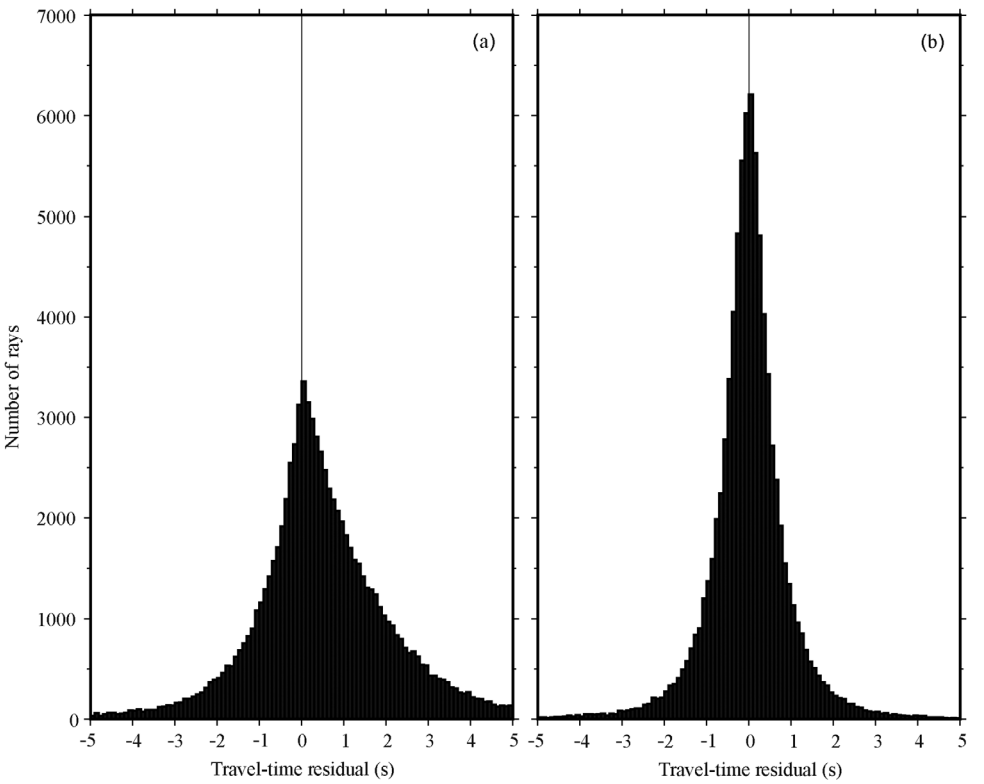

Figure 3. Distribution of local-event travel-time residuals (a) before and (b) after the earthquake relocation.

Moho (9–40 km) depths, the crustal thickness and velocities from the CRUST1.0 model are introduced into the starting velocity model, whereas the iasp91 model is adopted for the upper mantle velocities. A three-dimensional (3-D) grid is set up in the modelling space to express 3-D velocity variations. Considering the resolution limit of our data set and results of many synthetic tests conducted, we find that the optimal grid interval is 0.6° in the longitudinal and latitudinal directions, and we set grid meshes at depths of 5, 20, 50, 100, 150, 200, 250, 300, 400, 500, 600, and 700 km.

Before the 3-D velocity inversion, the 2749 local earthquakes are relocated using all the P and S wave arrival times and the Adaptive Quantum Genetic Algorithm (AQGA) [*Shi et al*., 2009] to obtain accurate hypocentral parameters for the tomographic inversion. Because earthquake location is a highly nonlinear inversion process, the event relocation results with the AQGA have some uncertainties, similar to the results obtained with any other relocation schemes. In order to obtain the optimal results, 10 independent relocations are performed for each earthquake with the same data set and searching parameters, among which the result with the minimum root-mean-square (RMS) travel-time residual is considered to be the optimal one. The searching ranges for the hypocentral parameters are set as follows: ±0.5° for the longitude and latitude, ±20 km or ±50 km for the focal depth if the original focal depth is shallower or deeper than 50 km, and ±2.0 s for the origin time. The searching precision is set as follows: 0.001° for the longitude and latitude, 0.1 km for the focal depth, and ±0.1 s for the origin time. The iteration number and the group population are 100 and 10, respectively. After the relocation, the RMS travel-time residual for the local events is reduced from 1.606 s to 0.938 s (Figure 3). Figure 2d shows the distribution of the local earthquakes along six vertical cross-sections before and after the relocation. We can see that the relocated hypocenters of the intermediate-depth earthquakes form a clearer Wadati-Benioff zone down to a depth of ∼200 km (Figure 2d).

We conducted a number of tomographic inversions with different values of the damping and smoothing parameters to examine the trade-off between the norm of the 3-D velocity model and the RMS travel-time residual. The optimal values of the damping and smoothing parameters are found to be 10.0 and 500.0, respectively (Figure 4), by considering the balance between the reduction of the RMS residual and the smoothness of the 3-D velocity model [*Eberhart-Phillips*, 1986; *Zhao*, 2015]. The RMS travel-time residual is

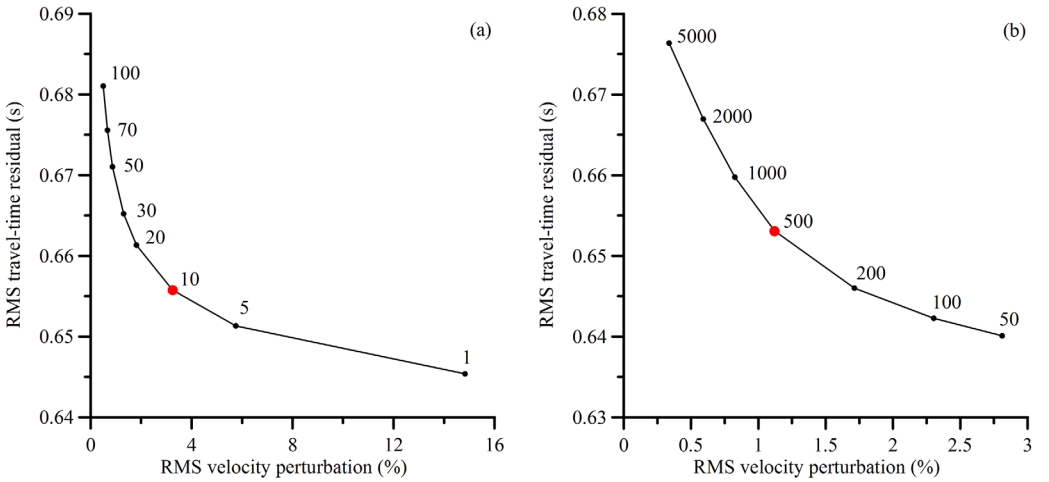

Figure 4. Trade-off curves for the root-mean-square (RMS) velocity perturbations and RMS travel-time residuals, with different values (the numbers beside the dots) of the damping parameter (a) and the smoothing parameter (b). The red dots denote the optimal values of the damping and smoothing parameters.

reduced from 0.938 s for the initial 1-D model to 0.650 s for the final 3-D model after the joint inversion of the local and teleseismic data.

4. Resolution Tests and Results

We conducted detailed checkerboard resolution tests (CRTs) for assessing the resolution of the obtained tomographic images [*Humphreys and Clayton*, 1988; *Zhao et al*., 1992]. Figure 5 shows the results of a CRT with a lateral grid interval of 0.6°. In the CRT, we first constructed an input checkerboard model by assigning velocity perturbations of ±3% to the 3-D grid nodes, and then calculated synthetic travel times with the same source-receiver geometry as in the observed data set. Random noise with a standard deviation of 0.1 s was added to the synthetic data. Finally, the synthetic arrival times are inverted for an output model using the same algorithm and the 1-D starting velocity model. By comparing the input checkerboard model with the output results, we can roughly estimate the resolution of the tomographic model. As shown in Figure 5, the 0.6° × 0.6° checkerboard pattern can be well recovered for most parts of the study region at depths of 5–300 km. In the deeper areas (300–700 km), the ray coverage is good and the resolution is higher for the eastern part of the study area, whereas the ray coverage is poor and the resolution is lower beneath Taiwan and Luzon Island (Figure 6). *Lévèque et al*. [1993] showed that in a CRT, larger-size structures may be poorly recovered even though the resolution is good at small scales. Accordingly, we conducted a CRT with a larger grid interval of 1.0° × 1.0°, and the test result is consistent with that for the smaller grid interval (0.6° × 0.6°), indicating that the checkerboard pattern can be recovered very well for most parts of the modeling space (Figure 7). Hence, we consider that main features of our tomographic images are reliable with a spatial resolution of 0.6° or greater.

The obtained tomographic images with a lateral grid interval of 0.6° are shown in Figures 8 and 9. The most prominent feature is a linear high-velocity (high-V) zone, which most likely reflects the subducted Eurasian Plate beneath the Luzon Arc. The high-V zone is coincident with the Wadati-Benioff zone, and it was also imaged by the previous regional and global tomographic studies [e.g., *Bijwaard et al*., 1998; *Lallemand et al*., 2001; *Wang et al*., 2006; *Wu et al*., 2007; *Zhao et al*., 2013; *Koulakov et al*., 2014].

Low-velocity (low-V) anomalies are revealed beneath the Taiwan and Luzon islands at depths of 5–50 km (Figures 8a–8c), suggesting that both of the islands have a thick crust. The tomographic images at depths of 100 and 150 km (Figures 8d and 8e) show clearly the slab-related high-V anomalies beneath the westernmost part of the Ryukyu Trench, Taiwan Island, Luzon Arc, and Luzon Island. These results are consistent with those of *Koulakov et al*. [2014], which may reflect the lithospheric collision of two oppositely oriented subducting slabs, i.e., the Eurasian Plate subducting beneath the Luzon Arc and the Philippine Sea Plate subducting beneath the Ryukyu Arc.

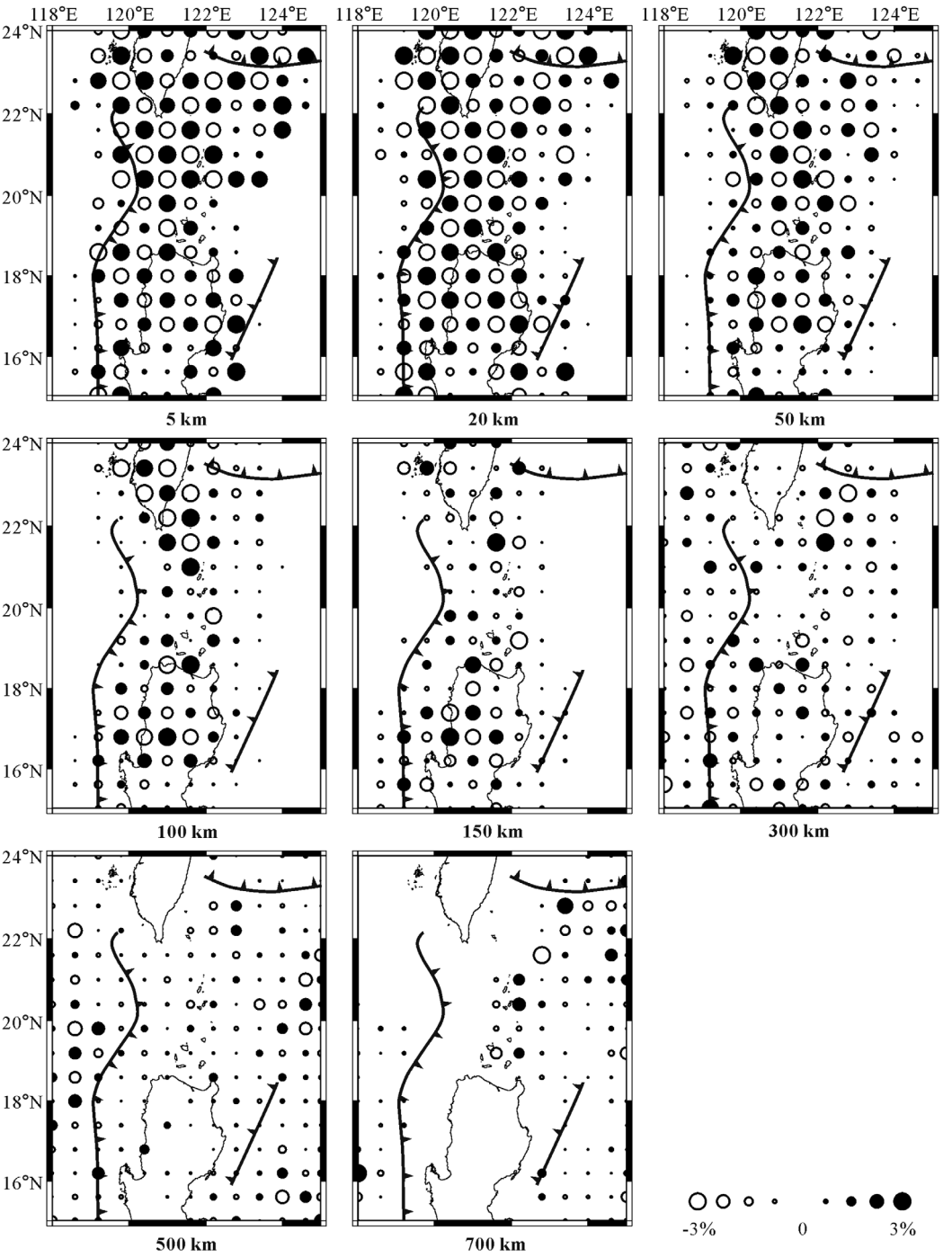

Figure 5. Results of a checkerboard resolution test for eight depth layers with a lateral grid interval of 0.6° in the longitudinal and latitudinal directions. The layer depth is shown below each map. The velocity perturbation scale is shown at the lower-right corner. The other symbols are the same as those in Figure 1.

In the vertical cross sections (Figure 9), the shape of the subducted plates represented by high-V anomalies appears to be highly variable. At 22°N (Figure 9a), southernmost of Taiwan Island, the subducted Eurasian Plate with a dip angle of ∼75° is not visible above ∼150 km depth in the upper mantle, instead a notable low-V zone (the patch outlined in red in Figure 9a) exists. In the deeper areas, however, the slab is clearly visible down to a depth of ∼500 km, which is similar to the image of the subducted Eurasian Plate beneath central and southern Taiwan revealed by *Wang et al.* [2006]. The low-V zone around the Manila Trench (the

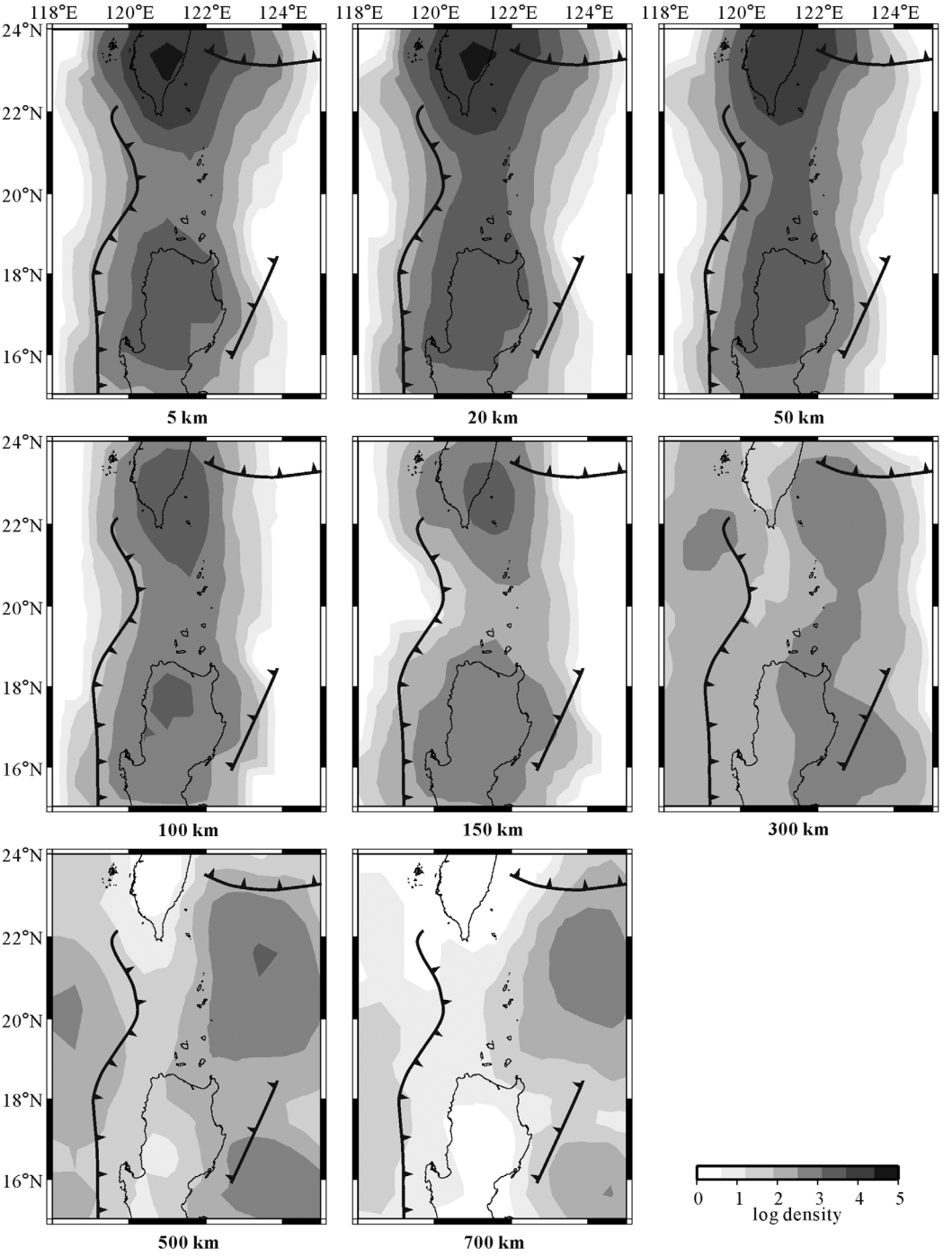

Figure 6. Ray density distribution in a logarithmic scale. The layer depth is shown below each map. The scale is shown at the lower-right corner. The other symbols are the same as those in Figure 1.

patch outlined in red in Figure 9a, also visible in map views at depths of 50–150 km in Figures 8c–8e) is possibly related to the transition from an area dominated by subduction to an area dominated by collision, which is discussed in the following section.

In the vertical cross section at 21°N (Figure 9b), the high-V anomaly representing the subducted Eurasian Plate is weak, extending down to ~200 km depth at a dip angle of ~45°. The Philippine Sea Plate is also imaged as a high-V zone with a thickness of ~120 km. At 20°N (Figure 9c), the Eurasian Plate subducts initially along the Manila Trench to ~250 km depth at a low angle of ~25°, and then changes to a higher dip

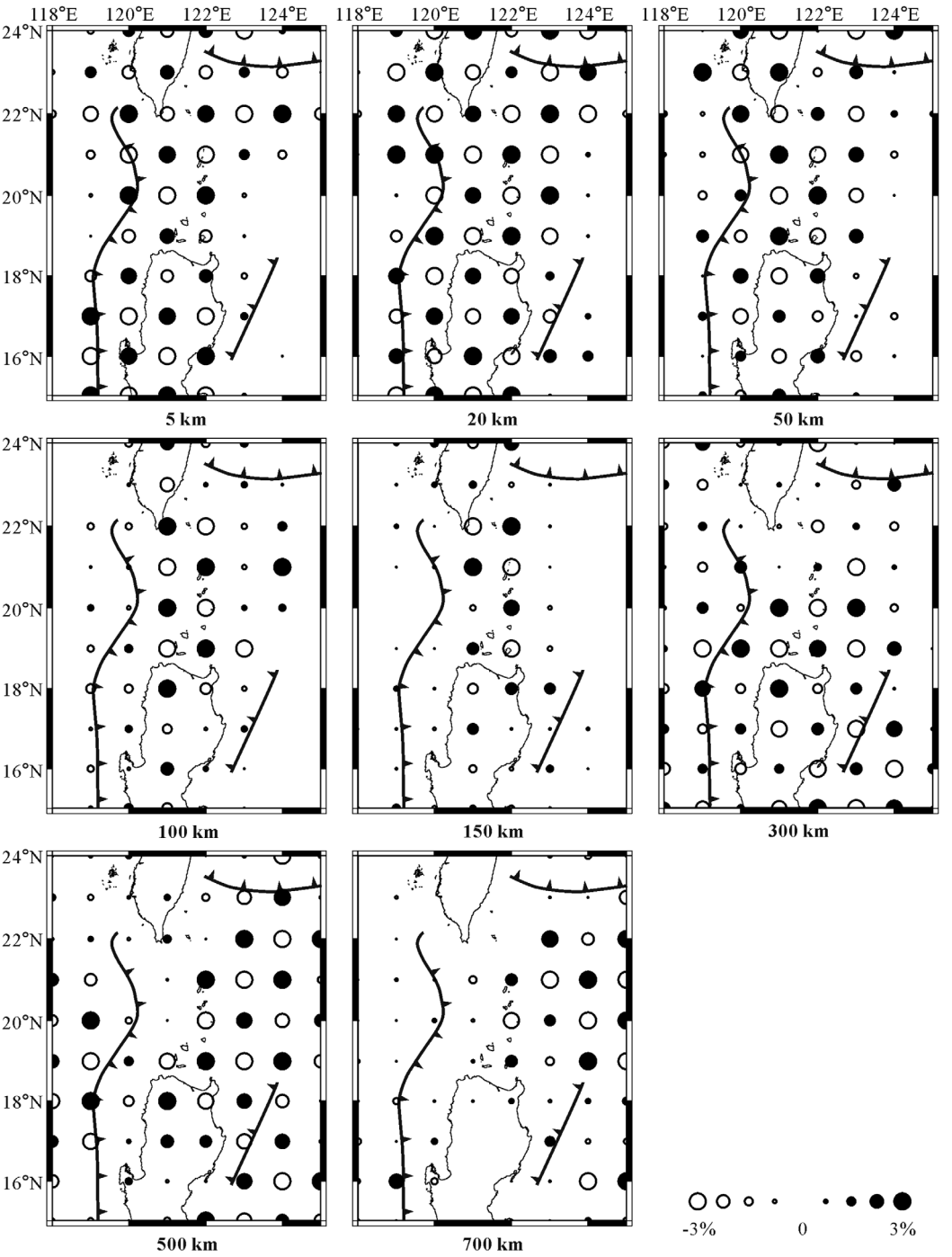

Figure 7. Results of a checkerboard resolution test for eight depth layers with a lateral grid interval of 1.0° in the longitudinal and latitudinal directions. The layer depth is shown below each map. The velocity perturbation scale is shown at the lower-right corner. The other symbols are the same as those in Figure 1.

angle (~75°) to ~500 km depth, which is slightly different from the tomographic results by *Fan et al.* [2015], whose images show that the subducted Eurasian Plate exhibits a horizontal feature above 100 km depth, which may be caused by the poorer hypocentral locations of local earthquakes in that study. At 19°N (Figure 9d), the subducted Eurasian Plate extends down to ~250 km depth with a dip angle of ~25°.

In the cross section at 18°N (Figure 9e), a nearly vertical Eurasian Plate is visible which could be overturned in the mantle transition zone (410–660 km depths) [*Lallemand et al.*, 2001; *Koulakov et al.*, 2014]. It is

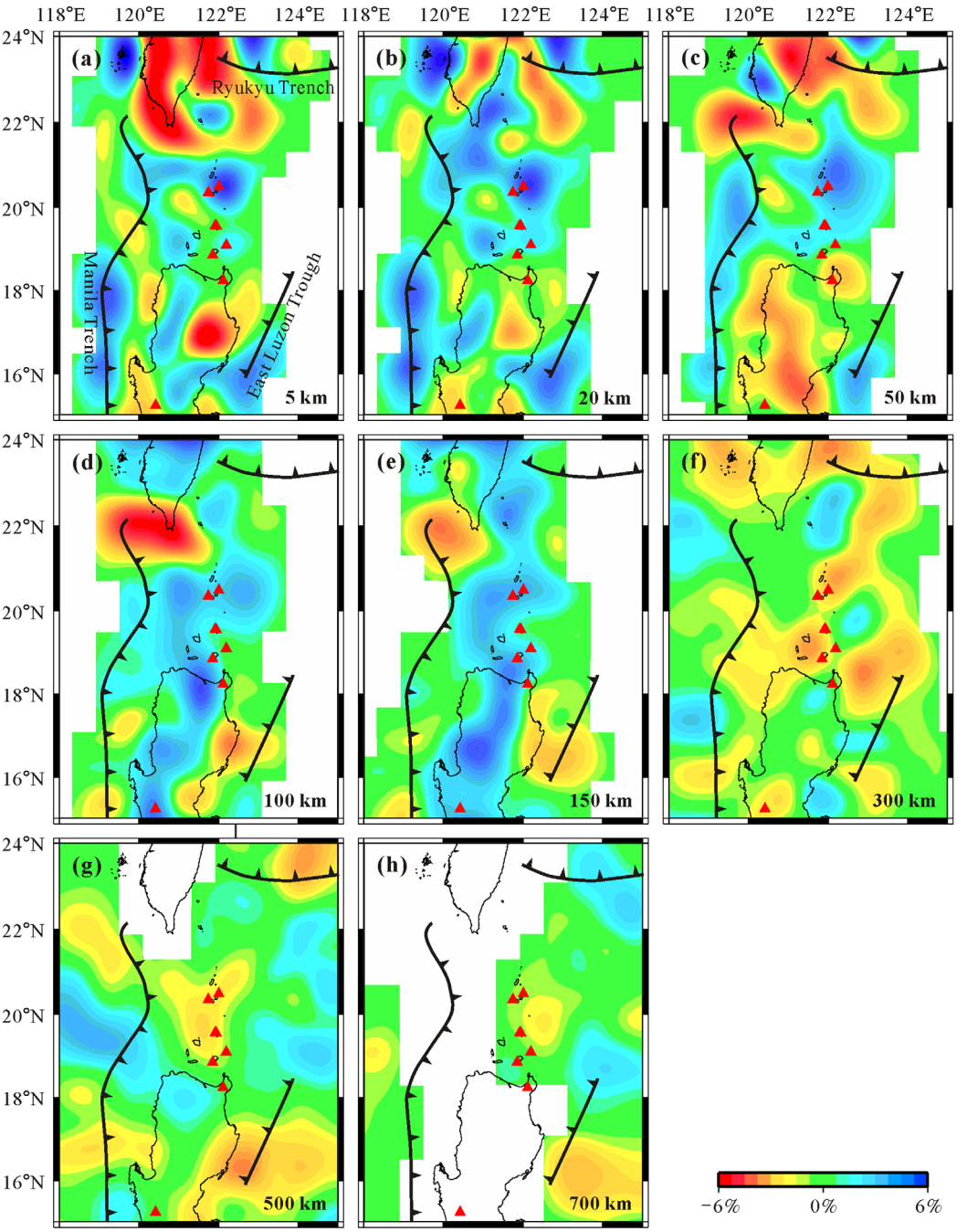

Figure 8. Map views of P-wave tomography. The depth layer is shown at the lower-right corner of each map. The red triangles denote the active volcanoes. The red and blue colors denote slow and fast velocity perturbations, respectively. The velocity perturbation scale is shown at the lower-right corner. The other symbols are the same as those in Figure 1.

noticeable that the subducted plate becomes aseismic below 100 km depth. At 17°N (Figure 9f), the image shows that the Eurasian Plate subducts to a depth of ~350 km with a low angle of ~32°. The low-V zones in the two sections (the patch outlined in red in Figures 9e and 9f) possibly indicate a tear in the subducted Eurasian Plate along the axis of the fossil ridge within the South China Sea and the formation of a slab window [*Fan and Wu*, 2014; *Fan et al*., 2015].

To confirm the morphology of the subducted Eurasian lithosphere revealed by our tomography, we conducted a model-recovery synthetic test. Figures 10a′–10f′ shows the synthetic input model which is constructed from the obtained tomographic images along different vertical cross sections (Figures 10a–10f). In

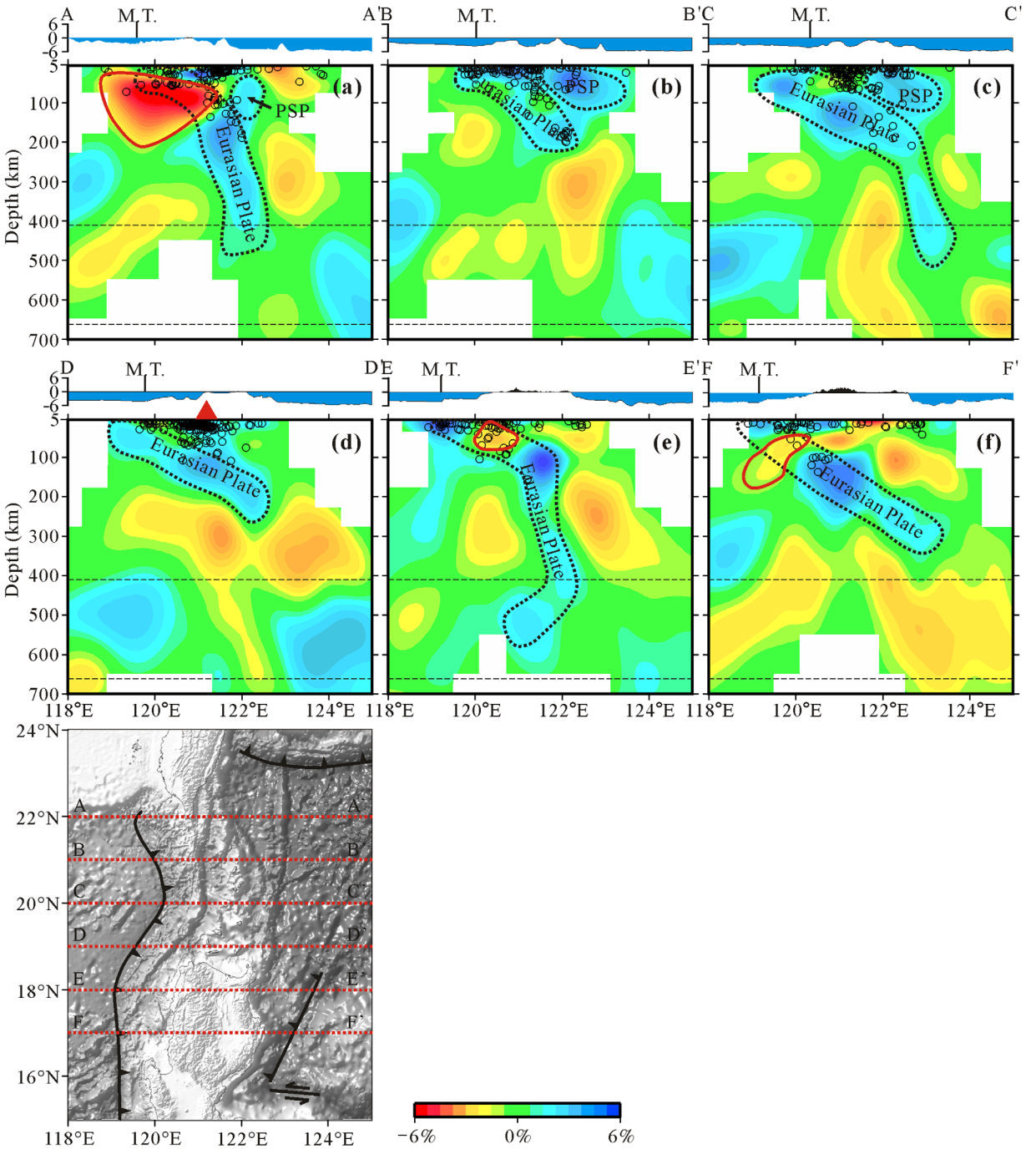

Figure 9. Vertical cross sections of P-wave tomography along the profiles shown on the inset map. The red and blue colors denote slow and fast velocity perturbations, respectively. The velocity perturbation scale is shown at the bottom. The open circles and red triangles show the earthquakes and active volcanoes, respectively, within a 30 km width of each profile. The black-dotted lines show the estimated morphology of the subducted Eurasian Plate. The black-dashed lines in each cross section denote the 410 and 670 km discontinuities. PSP, the Philippine Sea Plate.

the input model, the subducted slab has a +3% velocity perturbation relative to the surrounding mantle. Synthetic travel times are computed with the same source-receiver ray paths as in the real tomographic inversion. Random noise with a standard deviation of 0.1 s was also added to the synthetic data. Then the synthetic travel-time data are inverted for an output model which is shown in Figures 10a"–10f". The test results indicate that the input slab anomalies can be generally recovered, though smearing occurs at some depths because of the insufficient ray coverage and lower resolution there.

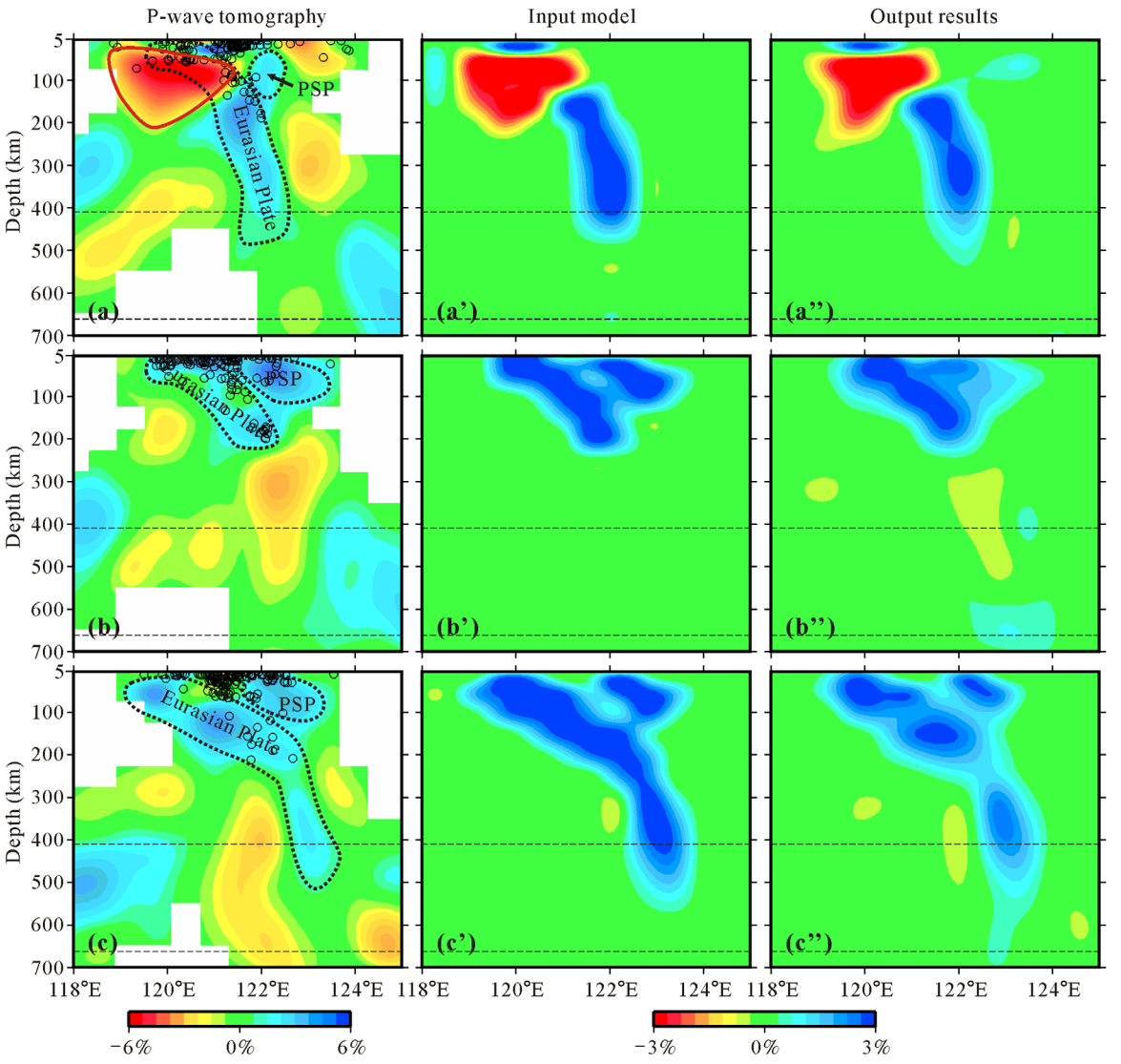

Figure 10. (a–f) The tomographic images obtained. (a′–f′) The input model and (a″–f″) output results of a restoring resolution test (see text for details). The other symbols are the same as those in Figure 9.

5. Discussion

5.1. Evidence for a Buoyant Plateau Subduction

The collision and/or subsequent subduction of a buoyant plateau is a common feature in the circum-Pacific subduction systems and have been demonstrated by many geophysical and geological studies (e.g., the Ogasawara Plateau) [*Mason et al.*, 2010]. However, the subduction of a buoyant plateau at the Manila Trench, which was first suggested by *Bautista et al.* [2001], has not been clearly demonstrated yet.

Our tomographic results reveal the 3-D morphology of the subducted Eurasian Plate along the northern segment of the Manila Trench. These profiles show that the dip angle of the subducted Eurasian Plate has large variations, from near-vertical at ~18°N, to a low value of ~25° above 250 km depth at ~20°N, and then to a high value of ~75° at ~22°N (Figure 9). The dramatic changes of the dip angle along the trench, especially the shallower angle at ~20°N, indicate that the buoyant plateau has partially subducted beneath the Luzon Arc contributing to the formation of the Hengchun Peninsula and the Hengchun submarine ridge [*McIntosh et al.*, 2013], rather than subduction of the normal oceanic crust at around 18°N [*Sibuet et al.*, 2002; *Hsu et al.*, 2004]. The small dip angle of the subducted Eurasian Plate with the buoyant plateau is consistent with the previous 3-D numerical simulations which show that a buoyant plateau can resist

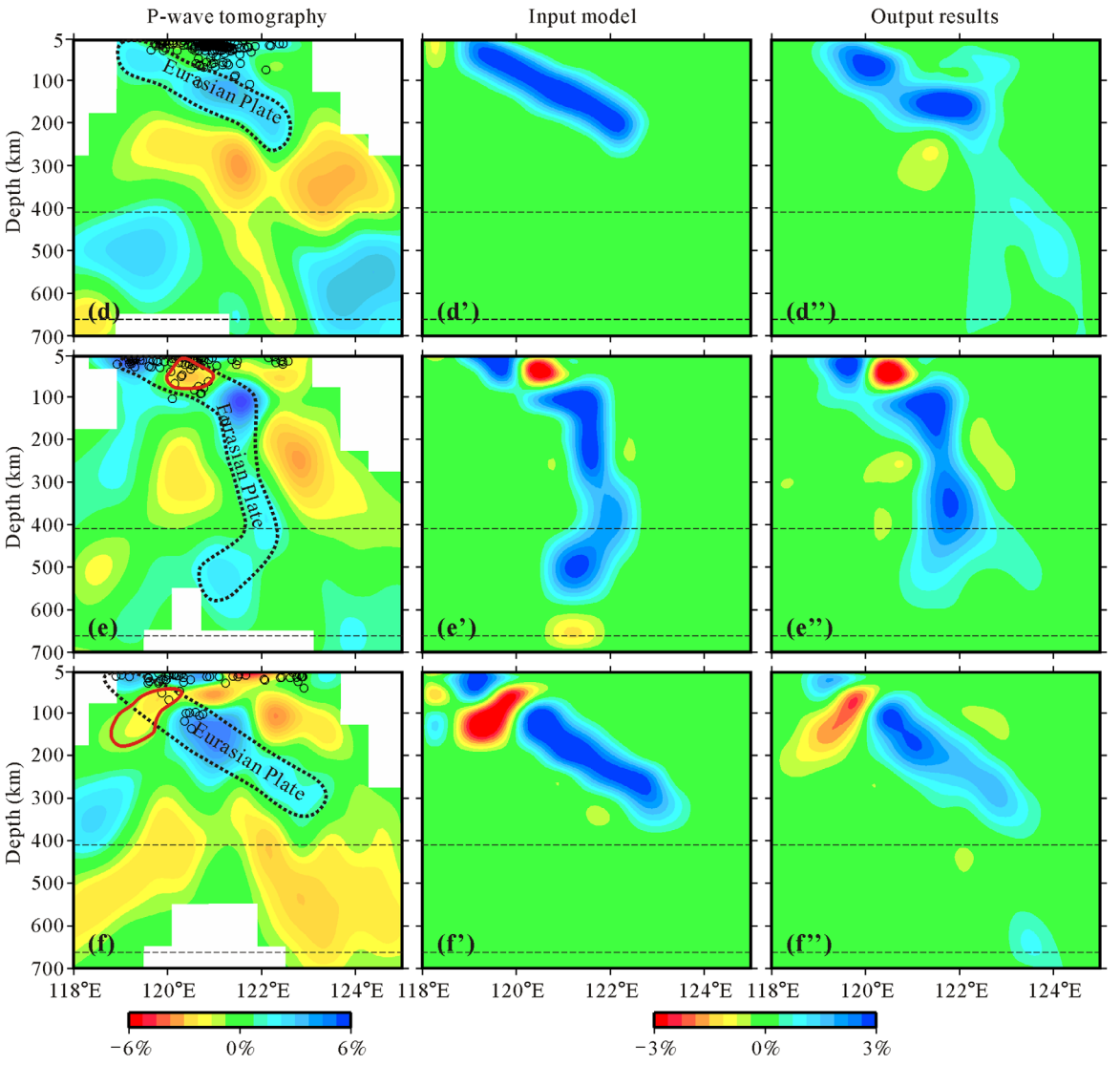

Figure 10. Continued.

subduction, with only a very small portion of the plateau becoming subducted along with the slab [e.g., *Mason et al.*, 2010].

According to the 3-D numerical simulations [e.g., *Mason et al.*, 2010], when the plateau collides with the trench and subsequently subducts beneath the overriding plate, a gap or tear can form in the subducted portion of the slab beneath the nonsubducting plateaus. Our tomographic images at ~19°N and ~21°N show that the subducted Eurasian Plate only exists down to a depth of ~250 km. The absence of the subducted slab at depths greater than ~250 km at ~19°N and ~21°N indicates that a slab tear exists at both sides of the buoyant plateau.

5.2. Geodynamic Implications

The collision of bathymetric highs, including buoyant plateaus with anomalously thick oceanic crust or pieces of continental crust, seamounts or seamount chains, and oceanic ridges, with the trench of a subduction zone can alter the trench behavior significantly [e.g., *Mason et al.*, 2010], which has been demonstrated by various numerical models. These variations could appear as an arcuate trench axis, reduction of the trench retreat rate and the slab dip [*Martinod et al.*, 2005, 2013; *Rosenbaum and Mo*, 2011], regional uplift of

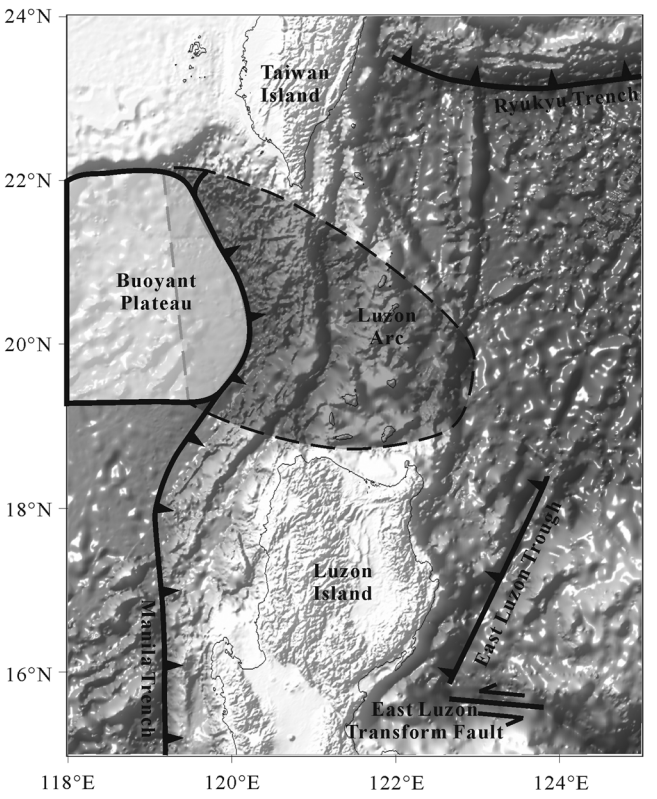

Figure 11. Projection of the subducted buoyant plateau (the gray shaded area) onto the surface, as inferred from the obtained tomographic images. The other symbols are the same as those in Figure 1.

the overriding plate [*Dominguez et al*., 1998, 2000], slab tearing [e.g., *Mason et al*., 2010], increased subduction erosion and a decrease in magma production [*Gerya et al*., 2009], and a rotation of the overriding plate [*Wallace et al*., 2009].

One of the most striking expressions of a buoyant plateau subduction is the formation of arc curvature and cusps [*Mason et al*., 2010], due to the arrival of relatively buoyant materials at the subduction zone to reduce locally the rate of subduction rollback seaward, and this in turn, could generate cusps and curvatures within the subduction system. The curvature of the trench axis in the Manila subduction zone at ~20°N could be explained by pinning due to subduction of the buoyant plateau [*Bautista et al*., 2001].

The Luzon Arc consists of two volcanic chains: the Western Volcanic Chain (WVC) and the Eastern Volcanic Chain (EVC) (Figure 1). These two distinct volcanic provinces were attributed to the subduction of the fossil ridge of the South China Sea by *Yang et al*. [1996]. *Bautista et al*. [2001] refined the model of *Yang et al*. [1996] by involving the collision and subsequent partial subduction of the buoyant plateau at around 20°N; however, they could not explain why the WVC and EVC are separated by ~50 km at ~18°N, while they converge into a single volcanic chain from ~20°N to southern Taiwan. Although the resolution of our present tomography is not high enough to image clearly low-V zones beneath the active volcanoes, the morphology of the subducted Eurasian Plate revealed by our tomography is consistent with the model of *Bautista et al*. [2001]. We suggest that the collision and subsequent partial subduction of the buoyant plateau composed of extended to hyperextended continental crust [*Eakin et al*., 2014] have induced the shallow dip of the subducted Eurasian Plate, causing the volcanic arc to migrate eastward. In addition, our tomographic results show that the subducted plate at ~21°N is slightly steeper than that at ~19°N. Therefore, we consider that the subducted buoyant plateau might be oriented NW-SE (Figure 11). Due to the oblique subduction at the Manila Trench caused by the northwestern movement of the Philippine Sea Plate, the two volcanic chains are separated by a distance of ~50 km at around 18°N, and then they gradually converge into a single volcanic chain northward.

At ~22°N, some TAIGER transects and multichannel seismic profiles have revealed a zone of very thin crust (~10 km thick) corresponding to a failed rifted continental crust, which defines the northwestern limit of the transitional crust [*McIntosh et al*., 2013]. This feature is consistent with our tomographic results which show a low-V zone at depths of 20–200 km beneath the Manila Accretionary Prism (Figure 9a, the patch outlined in red). A similar low-V anomaly was also revealed by *Wang et al*. [2009], which may be related to the accretionary prism. However, such a large low-V zone may not be associated only with the accretionary prism. The previous tomography has revealed the subducted Eurasian Plate down to a depth of ~300 km at ~23°N with a large dip angle and some low-V anomalies along the upper boundary of the subducted Eurasian Plate, which may reflect the subducted continental crust [*Wang et al*., 2009]. Consequently, the low-V zone in the vertical cross section at 22°N (Figure 9a) may indicate that the subduction along the Manila Trench stops there and the collision develops northward, which is also consistent with normal-faulting focal mechanisms in the lower crust of the Eurasian Plate [*Wu et al*., 2014].

Assuming that the plate convergence rate is constant at 8.2 cm/yr [*Yu and Kuo*, 1999] at ~20°N, it would take ~5 Ma and ~2.8 Ma for the subducted buoyant plateau to reach depths of ~250 km and ~100 km with a shallower dip angle of ~25°, which are consistent with the cessation time of the volcanoes in the WVC and the initiation time of volcanoes in the EVC south of 20°N [*Yang et al*., 1996]. These observations indicate that the buoyant plateau does not stop but merely slow down the subduction of the Eurasian Plate. The current phase of active orogenesis in Taiwan is generally assumed to have begun 5–6 Ma ago [e.g., *Teng*, 1990; *Castelltort et al*., 2011], which is concurrent with the initial subduction of the hypothesized buoyant plateau. These results suggest that the Taiwan Orogeny originates directly from the subduction of the buoyant plateau [*McIntosh et al*., 2013].

6. Conclusions

We have used high-resolution P-wave tomography to trace the subducted Eurasian Plate beneath the northern segment of the Manila Trench by simultaneously inverting 84,941 P-wave arrival times from 2749 local earthquakes and 7965 arrivals from 1462 teleseismic events. As a high-velocity zone, the subducted Eurasian Plate is revealed to exhibit a variety of morphology by our tomography. The angle and depth extent of the subducted slab vary along the trench: at 22°N, the slab subducts down to ~500 km depth at a high angle (~75°); at 21°N, the slab is visible down to ~200 km depth at a moderate angle (~45°); at 20°N, the slab subducts initially along the Manila Trench down to ~250 km depth at a low angle of ~25°, and then its dip angle changes to ~75° and the slab subducts down to ~500 km depth; at 19°N, the slab is visible down to ~250 km depth with a dip angle of ~25°; at 18°N, a nearly vertical slab is revealed which could be overturned in the mantle transition zone; and at 17°N, the slab becomes discontinuous and subducts down to a depth of ~350 km with a low angle of ~32°. The dramatic changes of the slab dip angle from the north to the south, especially its small angle at ~20°N, and the absence of the slab at depths $>$ 250 km at 19°N and 21°N, indicate partial subduction of a buoyant plateau beneath the Luzon Arc. The slab at ~21°N is slightly steeper than that at ~19°N, indicating that the subducted buoyant plateau is possibly oriented in a NW-SE direction, which may also explain why the western and eastern volcanic chains in the Luzon Arc are separated by ~50 km at ~18°N, whereas they converge into a single volcanic chain northward. The boundary between subduction in the south and collision in the north is possibly located at ~22°N, where a low-velocity zone is revealed at depths of 20–200 km beneath the Manila Accretionary Prism. The Taiwan Orogeny may originate directly from the subduction of the buoyant plateau because of their similar initial times.

Acknowledgments

We would like to thank Thorsten Becker (the Editor) and an anonymous reviewer for their thoughtful review comments which have improved the manuscript. We also thank the International Seismological Centre (ISC) and the Philippine Institute of Volcanology and Seismology for providing the P-wave arrival-time data of the local earthquakes and teleseismic events and the locations of the inactive and active volcanoes, respectively. All the figures in this article were plotted using the GMT software package [*Wessel and Smith*, 1998]. This work was financially supported by the National Natural Science Foundation of China (grant 41506059, 41476042) and the Strategic Priority Research Program of the Chinese Academy of Science (grant XDA11030102) to J. Fan and D. Dong, as well as research grants from Japan Society for the Promotion of Science (Kiban-S 23224012) and MEXT (Shin-Gakujutsu 26106005) to D. Zhao.

References

Bautista, B. C., M. L. C. Bautista, K. Oike, F. T. Wu, and R. S. Punongbayan (2001), A new insight on the geometry of subducting slabs in northern Luzon, Philippines, *Tectonophysics*, *339*, 279–310.

Beyssac, O., M. Simoes, J. P. Avouac, K. A. Farley, Y. G. Chen, Y. C. Chan, and B. Goffe (2007), Late Cenozoic metamorphic evolution and exhumation of Taiwan, *Tectonics*, *26*, TC6001, doi:10.1029/2006TC002064.

Bijwaard, H., W. Sparkman, and R. Engdahl (1998), Closing the gap between regional and global travel time tomography, *J. Geophis. Res.*, *103*, 30,055–30,078.

Castelltort, S., S. Nagel, F. Mouthereau, A. T. S. Lin, A. Wetzel, B. Kaus, S. Willett, S. P. Chiang, and W. Y. Chiu (2011), Sedimentology of early Pliocene sandstones in the south-western Taiwan foreland: Implications for basin physiography in the early stages of collision, *J. Asian Earth Sci.*, *40*(1): 52–71.

Dominguez, S., S. E. Lallemand, J. Malavieille, and R. von Huene (1998), Upper plate deformation associated with seamount subduction, *Tectonophysics*, *29*(3–4), 207–224.

Dominguez, S., J. Malavieille, and S. E. Lallemand (2000), Deformation of accretionary wedges in response to seamount subduction: Insights from sandbox experiments, *Tectonics*, *19*, 182–196.

Eakin, D. H., K. D. McIntosh, H. J. A. Van Avendonk, L. Lavier, R. Lester, C. S. Liu, and C. S. Lee (2014), Crustal-scale seismic profiles across the Manila subduction zone: The transition from intraoceanic subduction to incipient collision, *J. Geophys. Res. Solid Earth*, *119*, 1–17, doi: 10.1002/2013JB010395.

Eberhart-Phillips, D. (1986), Three-dimensional velocity structure in northern California Coast Ranges from inversion of local earthquake arrival times, *Bull. Seismol. Soc. Am. 76*, 1025–1052.

Fan, J. K., and S. G. Wu, (2014), P-wave seismic tomography of the Manila Subduction Zone [in Chinese], *Chin. J. Geophys.*, *57*(7), 2127–2137, doi:10.6038/cjg20140709.

Fan, J. K., S. G. Wu, and G. Spence (2015), Tomographic evidence for a slab tear induced by fossil ridge subduction at Manila Trench, South China Sea, *Int. Geol. Rev.*, *57*(5–8), 998–1013.

Gerya, T. V., D. Fossati, C. Cantieni, and D. Seward (2009), Dynamic effects of aseismic ridge subduction: Numerical modelling, *Eur. J. Mineral.*, *21*(3), 649–661.

Hayes, D. E., and S. D. Lewis (1984), A geophysical study of the Manila Trench, Luzon, Philippines: 1. Crustal structure, gravity, and regional tectonic evolution, *J. Geophys. Res.*, *89*, 9171–9195.

Hsu, S. K., Y. C. Yeh, W. B. Doo, and C. H. Tsai (2004), New bathymetry and magnetic lineations identifications in the Northernmost South China Sea and their tectonic implications, *Mar. Geophys. Res.*, *25*(1), 29–44.
Humphreys, E., and R. Clayton (1988), Adaptation of back projection tomography to seismic travel time problems, *J. Geophys. Res.*, *93*, 1073–1085.
Kaus, B. J. P., C. Steedman, and T. W. Becker (2008), From passive continental margin to mountain belt: Insights from analytical and numerical models and application to Taiwan, *Phys. Earth Planet. Inter.*, *171*, 235–251.
Kennett, B. L. N., and E. R. Engdahl (1991), Travel times for global earthquake location and phase identification, *Geophys. J. Int.*, *105*, 429–465.
Koulakov, I., Y. M. Wu, H. H. Huang, N. Dobretsov, A. Jakovlev, I. Zabelina, K. Jaxybulatov, and V. Chervov (2014), Slab interactions in the Taiwan region based on the P- and S- velocity distributions in the upper mantle, *J. Asian Earth Sci.*, *79*, 53–64, doi:10.1016/j.jseaes.2013.09.026.
Lallemand, S., Y. Font, H. Bijwaard, and H. Kao (2001), New insights on 3-D plates interaction near Taiwan from tomography and tectonic implications, *Tectonophysics*, *335*, 229–253.
Laske, G., G. Masters, Z. Ma, and M. Pasyanos (2013), Update on CRUST1.0 - A 1-degree Global Model of Earth's Crust, *Geophys. Res. Abstr*, *15*, 2013–2658.
Lee, Y. H., C. C. Chen, T. K. Liu, H. C. Ho, H. Y. Lu, and W. Lo (2006), Mountain building mechanisms in the Southern Central Range of the Taiwan Orogenic Belt-from accretionary wedge deformation to arc-continental collision, *Earth Planet. Sci. Lett.*, *252*, 413–422.
Lester, R., K. McIntosh, H. J. A. Van Avendonk, L. Lavier, C. S. Liu, and T. K. Wang (2013), Crustal accretion in the Manila trench accretionary wedge at the transition from subduction to mountain-building in Taiwan, *Earth Planet. Sci. Lett.*, *375*, 430–440.
Lévêque, J., L. Rivera, and G. Wittlinger (1993), On the use of the checker-board test to assess the resolution of tomographic inversions, *Geophys. J. Int.*, *115*, 313–318.
Liu, T. K., Y. G. Chen, W. S. Chen, and S. H. Jiang (2000), Rates of cooling and denudation of the early Penglai orogeny, Taiwan, as assessed by fission track constraints, *Tectonophysics*, *320*, 69–82.
Martinod, J., F. Funiciello, C. Faccenna, S. Labanieh, and V. Regard (2005), Dynamical effects of subducting ridges: Insights from 3-D laboratory models, *Geophys. J. Int.*, *163*, 1137–1150.
Martinod, J., B. Guillaume, N. Espurt, C. Faccenna, F. Funiciello, and V. Regard (2013), Effect of aseismic ridge subduction on slab geometry and overriding plate deformation: Insights from analogue modeling, *Tectonophysics*, *588*, 39–55.
Mason, W. G., L. Moresi, P. G. Betts, and M. S. Miller (2010), Three-dimensional numerical models of the influence of a buoyant oceanic plateau on subduction zones, *Tectonophysics*, *483*(1–2), 71–79.
McIntosh, K., H. van Avendonk, L. Lavier, W. R. Lester, D. Eakin, F. Wu, C. S. Liu, and C. S. Lee (2013), Inversion of a hyper-extended rifted margin in the southern Central Range of Taiwan, *Geology*, *41*(8), 871–874.
Paige, C. C., and M. A. Saunders (1982), LSQR: An algorithm for sparse linear equations and sparse least squares, *ACM Trans. Math. Software*, *8*, 43–71.
Rangin, C., W. Spakman, M. Pubellier, and H. Bijwaard (1999), Tomographic and geological constraints on subduction along the eastern Sundaland continental margin (South-East Asia), *Bull. Soc. Geol. Fr.*, *170*(6), 775–788.
Rosenbaum, G., and W. Mo (2011), Tectonic and magmatic responses to the subduction of high bathymetric relief, *Gondwana Res.*, *19*(3), 571–582.
Shi, X. M., J. K. Fan, H. M. Luo, M. Xiao, G. S. Yang, and X. H. Zhang (2009), Adaptive quantum genetic inversion algorithm for one-dimensional magnetotelluric inverse problem, *Earth Sci.*, *34*(4), 691–698.
Sibuet, J. C., S. K. Hsu, X. Le Pichon, J. R. Le Formal, D. Reed, G. Moore, and C. S. Liu (2002), East Asia plate tectonics since 15 Ma: Constraints from the Taiwan region, *Tectonophysics*, *344*(1–2), 103–134.
Smith, W. H. F., and D. T. Sandwell (1997), Global seafloor topography from satellite altimetry and ship depth soundings, *Science*, *277*, 1957–1962.
Stephan, J. F., R. Blanchet, C. Rangin, B. Pelletier, J. Letouzey, and C. Muller (1986), Geodynamic evolution of the Taiwan-Luzon-Mindoro belt since the late Eocene, *Tectonophysics*, *125*, 245–268, doi:10.1016/0040-1951(86)90017-X.
Suppe, J. (1981), Mechanics of mountain building and metamorphism in Taiwan, *Geol. Soc. Chin. Memoir.*, *4*, 67–89.
Suppe, J. (1984), Kinematics of arc-continent collision, flipping of subduction, and back-arc spreading near Taiwan, *Geol. Soc. Chin. Memoir.*, *6*, 21–33.
Suppe, J. (1988), Tectonics of arc-continent collision on both sides of the South China Sea: Taiwan and Mindoro, *Acta Geol. Taiwan*, *26*, 1–18.
Taylor, B., and D. E. Hayes (1983), Origin and history of the South China Sea basin, in *The Tectonic and Geologic Evolution of Southeast Asian Seas and Islands: Part 2, Geophys. Monogr. Ser.*, vol. 27, edited by D. E. Hayes, pp. 23–56, AGU, Washington, D. C., doi:10.1029/GM027p0023.
Teng, L. S. (1990), Geotectonic evolution of Late Cenozoic arc continent collision in Taiwan, *Tectonophysics*, *183*, 57–76, doi:10.1016/0040-1951(90)90188-E.
Wallace, L. M., S. Ellis, and P. Mann (2009), Collisional model for rapid fore-arc block rotations, arc curvature, and episodic back-arc rifting in subduction settings, *Geochem. Geophys. Geosyst.*, *10*, *Q05001*, doi:10.1029/2008GC002220.
Wang, Z., D. Zhao, J. Wang, and H. Kao (2006), Tomographic evidence for the Eurasian lithosphere subducting beneath south Taiwan, *Geophys. Res. Lett.*, *33*, L18306, doi:10.1029/2006GL027166.
Wang, Z., Y. Fukao, D. Zhao, S. Kodaira, O. P. Mishra, and A. Yamada (2009), Structural heterogeneities in the crust and upper mantle beneath Taiwan, *Tectonophysics*, *476*, 460–477.
Wessel, P., and W. Smith (1998), New, improved version of generic mapping tools released, *Eos Trans. AGU*, *79*, 579.
Willett, S. D., D. Fischer, C. Fuller, E. C. Yeh, and C. Y. Lu (2003), Erosion rates and orogenic-wedge kinematics in Taiwan inferred from fission track thermochronometry, *Geology*, *31*(11), 945–948.
Wu, F. T., R. J. Rau, and D. Salzberg (1997), Taiwan Orogeny; thin-skinned or lithospheric collision? An introduction to active collision in Taiwan, *Tectonophysics*, *274*, 191–220.
Wu, F. T., H. Kuo-Chen, and K. D. McIntosh (2014), Subsurface imaging, TAIGER experiments and tectonic models of Taiwan, *J. Asian Earth Sci.*, *90*, 173–208.
Wu, Y. M., C. H. Chang, L. Zhao, J. B. H. Shyu, Y. G. Chen, K. Sieh, and J. P. Avouac (2007), Seismic tomography of Taiwan: Improved constraints from a dense network of strong-motion stations, *J. Geophys. Res.*, *112*, B08312, doi:10.1029/2007JB004983.
Yang, T. F., T. Lee, C. H. Chen, S. N. Cheng, U. Knittel, R. S. Punongbayan, and A. R. Rasdas (1996), A double island arc between Taiwan and Luzon: Consequence of ridge subduction, *Tectonophysics*, *258*, 85–101.

Yu, S. B., and L. C. Kuo (1999), GPS observation of crustal deformation in the Taiwan-Luzon region, *Geophys. Res. Lett.*, *26*, 923–926.
Zhao, D. (2015), *Multiscale Seismic Tomography*, 304 pp., Springer.
Zhao, D., A. Hasegawa, and S. Horiuchi (1992), Tomographic imaging of P and S wave velocity structure beneath northeastern Japan, *J. Geophys. Res.*, *97*, 19,909–19,928.
Zhao, D., A. Hasegawa, and H. Kanamori (1994), Deep structure of Japan subduction zone as derived from local, regional, and teleseismic events, *J. Geophys. Res.*, *99*, 22,313–22,329.
Zhao, D., T. Yanada T, A. Hasegawa, N. Umino, and W. Wei (2012), Imaging the subducting slabs and mantle upwelling under the Japan Islands, *Geophys. J. Int.*, *190*, 816–828.
Zhao, D., Y. Yamamoto, and T. Yanada (2013), Global mantle heterogeneity and its influence on teleseismic regional tomography, *Gondwana Res.*, *23*, 595–616.